Admissible Diffusion Wavelets and Their Applications in Space-Frequency Processing

Tingbo Hou, *Student Member*, *IEEE*, and Hong Qin, *Senior Member*, *IEEE*

Abstract—As signal processing tools, diffusion wavelets and biorthogonal diffusion wavelets have been propelled by recent research in mathematics. They employ diffusion as a smoothing and scaling process to empower multiscale analysis. However, their applications in graphics and visualization are overshadowed by nonadmissible wavelets and their expensive computation. In this paper, our motivation is to broaden the application scope to space-frequency processing of shape geometry and scalar fields. We propose the admissible diffusion wavelets (ADW) on meshed surfaces and point clouds. The ADW are constructed in a bottom-up manner that starts from a local operator in a high frequency, and dilates by its dyadic powers to low frequencies. By relieving the orthogonality and enforcing normalization, the wavelets are locally supported and admissible, hence facilitating data analysis and geometry processing. We define the novel rapid reconstruction, which recovers the signal from multiple bands of high frequencies and a low-frequency base in full resolution. It enables operations localized in both space and frequency by manipulating wavelet coefficients through space-frequency filters. This paper aims to build a common theoretic foundation for a host of applications, including saliency visualization, multiscale feature extraction, spectral geometry processing, etc.

Index Terms—Diffusion wavelets, wavelet analysis, feature extraction, space-frequency processing

1 Introduction

Recent years have witnessed the rapid development of wavelet tools and algorithms on manifolds. Wavelets have the powerful localization property in both frequency and space. They have been widely employed to tackle many problems of visualization and graphics, such as image operations [1], image segmentation [2], image-based rendering [3], volume rendering [4], scientific visualization [5], spectral rendering [6], multiresolution for surfaces [7], mesh compression [8], and animation compression [9]. Nevertheless, most existing wavelets are constructed either on regular domain or via explicit subdivision, followed by predominant applications in multiresolution analysis (MRA). In this paper, we are directly inspired by the powerful functionality of frequency-domain processing. One such example is the manifold harmonics transform (MHT) [10], an analogue of the Fourier transform on manifolds. Although the Fourier transform has the attractive localization property in frequency, it is incapable of localizing signals in space (or time). This drawback undoubtedly overshadows many potential applications that demand local operations on fine details. Thus, challenges still prevail in bridging wavelets and the space-frequency processing on manifold geometry.

Wavelets on meshed surfaces have been extensively studied for more than a decade with remarkable accomplishment so far. Conventional methods are build upon explicit subdivision schemes [11], [12], [13], [14], [15], [16], [17], [18], which can directly dilate functions in frequency, and regularly downsample the space. The essential motivation is to apply the MRA to arbitrary surfaces. The subdivision seeks to model a smooth surface via a recursive process of refining polygonal faces from a coarse base mesh, which is essentially a model-driven, top-down methodology toward wavelets definition and construction. The subdivision wavelets have been frequently used for geometry compression and level-of-detail data visualization. It requires constructing the subdivision hierarchy before defining wavelets, which limits its application scope. Nowadays, in conjunction with the rapid technology advancement of data acquisition and computing power, many graphics problems call for a paradigm shift from model driven to data driven. The regularly refined hierarchy is computationally expensive and perhaps even harder to build. Consequently, it gives rise to strong demand in flexibly adapted wavelet tools without building the subdivision explicitly, which can be used for fast space-frequency processing. Applications (that are critically enabled) span traditional geometry processing to visual analytics, feature extraction, feature-driven data mapping, etc., many of which require local operations on fine details at different frequencies.

Recently, a new methodology to construct wavelets on manifolds (i.e., the diffusion wavelets (DW) [19]) has been proposed. In sharp contrast to the aforementioned subdivision wavelets, the diffusion wavelets are built by a fundamentally different, bottom-up philosophy that starts from the fine input data. The construction adopts a diffusion operator and its powers to expand the nested subspaces, where scaling functions and wavelets are obtained by orthogonalization and rank-revealing compression. This diffusion-driven methodology naturally dilates the functions associated with the underlying heat diffusion process, which solely depends on manifold geometry. It allows flexible construction directly from data. However, the constructed scaling functions and wavelets are not locally supported,

• *The authors are with the Department of Computer Science, Stony Brook University, Computer Science Building, Stony Brook, NY 11794-4400. E-mail: {thou, qin}@cs.stonybrook.edu.*

Manuscript received 22 Sept. 2011; revised 20 Feb. 2012; accepted 29 Mar. 2012; published online 10 Apr. 2012.
Recommended for acceptance by L. Kobbelt.
For information on obtaining reprints of this article, please send e-mail to: tvcg@computer.org, and reference IEEECS Log Number TVCG-2011-09-0232.
Digital Object Identifier no. 10.1109/TVCG.2012.111.

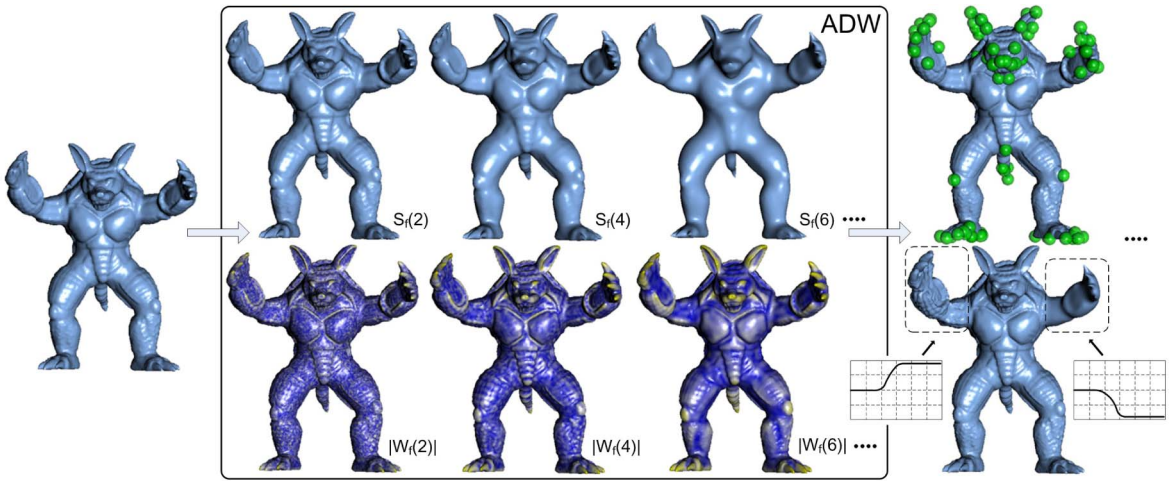

Fig. 1. The framework of our method. By the ADW, a shape is transformed to scaling coefficients $\mathcal{S}_f$ visualized as smoothed shapes and wavelet coefficients $\mathcal{W}_f$ visualized as coded colors. Examples highlight the application-relevant results. In the example of feature extraction, multiscale features are shown as green balls. In the example of geometry processing, one arm of the Armadillo is smoothed while the other is enhanced.

which limits the functionality of space localization. In fact, it is impossible to construct wavelets that are simultaneously fully orthogonal, locally supported, and symmetric [16]. The biorthogonal diffusion wavelets (BDW) [20] relieved the excessively strict orthogonality property of scaling functions. However, neither the DW transform nor the BDW transform explicitly satisfies the admissibility condition. The admissibility condition and local support property make wavelets oscillating and attenuated on the domain. Moreover, their constructions require expensive operations of QR decomposition and matrix inverse. The rank-revealing QR decomposition downsamples the subspaces to keep the scaling functions with full ranks. Consequently, the inverse transform is carried out by orthogonal or biorthogonal basis at each frequency, which is inconvenient for spectral processing in multiple frequencies.

In this paper, we propose the admissible diffusion wavelets (ADW), which are founded upon the diffusion wavelets yet derived from a fundamentally different formulation. We adopt the bottom-up approach to construct the subspaces by a diffusion operator and its dyadic powers. Through mathematical rigor, we formulate the scaling functions and wavelets that are locally supported. Different with the DW and the BDW, our wavelets are formulated as differences of adjacent scaling functions with zero means. The attenuated oscillation satisfies the admissibility condition. For the purpose of fast space-frequency processing, we propose the rapid reconstruction. It recovers the signal from multiple bands of high frequencies and a low-frequency base, all of which are in full resolution. As a result, we are able to avoid the expensive QR decomposition, and immediately proceed with the fast spectral processing. Through algorithmic development and experimental validation, we showcase applications of the ADW in spectral analysis, including saliency visualization, feature definition and extraction, and geometry processing. Fig. 1 illustrates the framework of our method. By the ADW, a shape is transformed to scaling coefficients $\mathcal{S}_f$ visualized as smoothed shapes and wavelet coefficients $\mathcal{W}_f$ visualized as coded colors. Examples are shown to portray the application-relevant results. In the example of feature extraction, multiscale features are shown as green balls. In the example of local geometry filtering, one arm of the Armadillo is smoothed while the other is enhanced. Specifically, the contributions of this paper include

- We rigorously formulate the ADW on meshed surfaces and point clouds, which are locally supported and admissible.
- We articulate the rapid reconstruction, which recovers the signal from multiple bands of high frequencies and a low-frequency base. It enables local space-frequency processing by analyzing and manipulating wavelet coefficients.
- We apply the ADW transform to various tasks of spectral analysis, including saliency visualization, multiscale feature extraction, and geometry processing. Our experiments broaden its application scope, demonstrating it as powerful and efficient tools in data visualization and modeling.

2 Related Work

This section briefly reviews the previous work of adapted Fourier transform, subdivision wavelets, and diffusion wavelets, on manifold geometry.

2.1 Adapted Fourier Transform

Processing in spectral domain offers flexible operations for shape geometry. In [21], the 2D discrete Fourier transform was applied to local patches constructed from point-sampled geometry. Later, eigenfunctions of the symmetric Laplacian of the connectivity graph were adopted for spectral processing [22], [23], [24]. The processing is achieved by projecting the shape geometry onto an orthonormal basis, which, however, is derived from the mesh topology but not the manifold. Analogous to Fourier basis for euclidean domain signals, manifolds have similar orthogonal basis formed by Laplace-Beltrami eigenfunctions [25]. Assume the Laplace-Beltrami operator Δ has the eigensystem $\{\lambda_k, \phi_k\}_{k=0}^{\infty}$: $\Delta\phi_k = \lambda_k\phi_k$, where λ_k is the kth eigenvalue associated with the eigenvector ϕ_k. The spectrum

of Δ consists of an increasing positive sequence $\{\lambda_k\}_{k=0}^{\infty}$. The eigenfunctions (i.e., manifold harmonics) $\{\phi_k\}_{k=0}^{\infty}$ form an orthonormal basis in the Hilbert space $L^2(M)$. They repetitively oscillate on the manifold with similar behaviors like sine and cosine functions. Vallet and Lévy [10] defined the manifold harmonic transform of a function f by the inner product $\mathcal{F}_f(k) = \langle f, \phi_k \rangle$, where k is related to the "frequency." Since the manifold harmonics basis (MHB) is orthogonal, the inverse transform can be computed by $f = \sum_{k=0}^{\infty} \langle f, \phi_k \rangle \phi_k$. In [26], Rong et al. employed spectral decomposition to perform mesh editing on the base domain with low frequencies and reconstruct details with high frequencies. The Laplace-Beltrami eigenfunctions have nice properties in spectral analysis. However, thousands of eigenfunctions are needed for preserving details of large meshes, which typically demand tremendous computation time and memory. Furthermore, similar to the Fourier basis, the eigenfunctions do not have localization in space domain, which implies that all processes are uniformly operated on the entire manifold. These drawbacks severely limit its application power in mesh editing and geometry processing.

2.2 Subdivision Wavelets

One natural construction of wavelets on manifolds can be achieved via explicit subdivision. The subdivision wavelet was originally proposed by Lounsbery et al. [16]. The subdivision scheme that iteratively refines the mesh geometry also refines the functions. The constructed wavelets are biorthogonal and locally supported. The subdivision wavelets rely on the subdivision connectivity of the mesh, which restricts the application scope to data compression and level-of-detail rendering. Guskov et al. [11] first generalized basic signal processing tools to triangular meshes with irregular connectivity, through subdivision wavelets. Daubechies et al. [27] studied subdivision wavelets built on irregular point sets. In [12], Bertram et al. utilized bicubic B-spline subdivision to construct wavelet transform that affords boundary curves and sharp features. In [13], B-spline wavelets were combined with the lifting scheme for biorthogonal wavelet construction. As a drawback, the subdivision wavelet requires the meshes to have subdivision connectivity, where remeshing process is frequently needed. To avoid remeshing, Valette and Prost [18] extended the subdivision wavelet for triangular meshes using irregular subdivision scheme that can be directly computed on irregular meshes. On spherical domains, Haar wavelets [14], [17] were constructed over nested triangular grids generated by subdivision. Recently, the spherical Haar wavelet basis was improved to the SOHO wavelet basis [15] that is both orthogonal and symmetric. In subdivision wavelets, the dilation of scaling functions strictly follows the subdivision scheme, which depends on the meshing. In [28], a biorthogonal wavelet analysis based on the $\sqrt{3}$-subdivision was proposed. It is a well-orchestrated solution on triangular meshes since the $\sqrt{3}$-subdivision is of the slowest topological refinement among all the traditional triangular subdivisions. In a recent work [29], Charina et al. constructed compactly supported tight frames of multivariate multiwavelets with subdivision schemes.

2.3 Diffusion Wavelets

In mathematics, Coifman and Maggioni [19] proposed the diffusion wavelets that use a diffusion operator and its dyadic powers for dilation. The nested subspaces are constructed as

$$L^2(M) = V_0 \supseteq V_1 \supseteq \cdots \supseteq V_k \supseteq \cdots$$

by continuously applying dyadic powers of the diffusion operator. Wavelets in the complement subspace W_k are subject to $V_{k-1} = V_k \oplus^{\perp} W_k$. The diffusion wavelets have many attractive properties. For example, the scaling and wavelet functions are fully orthogonal and complete. The orthogonality of basis induces the orthogonal decomposition of functions, which guarantees the best approximations in multiresolution analysis. Because of the orthogonality, the inverse transform has the same bases with the wavelet transform. The construction does not need subdivision, leading to great flexibility in practical use. The major drawback of diffusion wavelets is that, the scaling and wavelet functions are not locally supported. In fact, it is impossible to construct wavelets that are simultaneously fully orthogonal, locally supported, and symmetric [16]. In [20], Maggioni et al. proposed *biorthogonal* diffusion wavelets that are locally supported by relieving the orthogonality requirement. In [30], diffusion wavelets were adopted to approximate scalar-valued functions based on analyzing the structure and topology of the state space. Rustamov [31] studied the relation between mesh editing and diffusion wavelets by introducing the generalized linear editing (GLE). Recently, Hammond et al. [32] proposed the spectral method to construct wavelets on graphs. The wavelets are represented by a generating kernel and the eigenfunctions of the Laplace operator.

3 Admissible Diffusion Wavelets

This work is originally inspired by the DW. Whereas, we define our admissible diffusion wavelets in a significantly different formulation, with our unique emphasis in fast space-frequency processing.

3.1 Local Operator

Similar to the DW, our admissible wavelets are constructed in a bottom-up manner that starts from a local operator $\mathbf{T}$ and expands via its dyadic powers. For a meshed surface M, our wavelet operator forms a matrix with rows defined as functions at the associated vertices

$$\begin{cases} \mathbf{T}(x,y) = A(y) \exp\left(-\dfrac{\|x-y\|^2}{4t}\right) \\ \mathbf{T}(x,x) = \displaystyle\sum_{y \in M} \mathbf{T}(x,y), \end{cases} \tag{1}$$

where $A(y)$ is the vertex area of y, and t is a fixed quantity. It can be interpreted as a transition matrix of a random walk, which measures the probability of a one-step random walk moving from x to y on M. This explains that our wavelet operator has a diffusion-type distribution, which spreads from a vertex to its neighbors according to their distances. The quantity t corresponds to the neighborhood size. In this

work, we let $t = E^2/2$ where E is the mean edge length of mesh M. In this way, only a few neighboring entries $\mathbf{T}(x, y)$ for vertex x have nonzero values, while other entries are all becoming zero. This indicates that $\mathbf{T}$ is a highly sparse matrix. For a uniformly sampled mesh, the operator $\mathbf{T}$ is approximately symmetric, since vertex areas are close.

This operator is closely related to the discrete Laplace operator $\mathbf{L}$ in [33], with an explicit expression:

$$\mathbf{T} = 4\pi t^2(\mathbf{L} - 2D_{\mathbf{L}}), \tag{2}$$

where $D_{\mathbf{L}}$ is the diagonal matrix with $D_{\mathbf{L}}(x, x) = \mathbf{L}(x, x)$. According to the algorithm for computing the Laplace operator on point clouds [34], the proposed operator $\mathbf{T}$ can be applied to point clouds. For each point, we seek 10 nearest neighbors, only which are involved in nonzero entries of the operator. The quantity E here for computing t is then approximated by averaging the distances with these neighbors.

3.2 Scaling Functions and Wavelets

In the diffusion wavelets, the dyadic powers of a diffusion operator are employed to smooth the function space $L^2(M)$. Decomposed from the dyadic powers, scaling functions form an orthogonal and complete basis in each subspace. The powers have decreasing ranks; therefore, the space is compressed. By dropping the orthogonality, the biorthogonal diffusion wavelets improve the scaling functions to be locally supported. However, they still need the rank-revealing QR decomposition to compress the function space. The scaling matrix has a full rank, and is biorthogonal.

We adopt this bottom-up approach but with a significantly different formulation when defining wavelets. Initially, the function space has a canonical basis $\Phi_0 = \{\varphi_{0,x}\}_{x\in M}$ of delta functions:

$$\varphi_{0,x}(y) = \delta_x(y). \tag{3}$$

In the first level, the scaling functions $\Phi_1 = \{\varphi_{1,x}\}_{x\in M}$ are dilated once by $\mathbf{T}$, given by

$$\Phi_1 = [\Phi_0\mathbf{T}]_r, \tag{4}$$

where $[\cdot]_r$ denotes the row-based normalization

$$\varphi_{1,x} = \frac{\mathbf{T}(x, \cdot)}{\|\mathbf{T}(x, \cdot)\|_1}. \tag{5}$$

Following this paradigm, the scaling functions in the jth level $\Phi_j = [\Phi_{j-1}\Phi_{j-1}]_r$ are constructed by the square of scaling functions in the $(j-1)$th level

$$\varphi_{j,x} = [\varphi_{j-1,x}\Phi_{j-1}]_r. \tag{6}$$

They are dilated by $\mathbf{T}^{2^{j-1}}$ subject to row-based normalization. The constructed scaling functions are locally supported, with the following properties:

$$\varphi_{j,x}(y) \geq 0, \text{ and } \sum_{y\in M} \varphi_{j,x}(y) = 1. \tag{7}$$

The dyadic powers $\mathbf{T}^{2^j}$ decrease in rank as j increases, which indicates a compression of the function space. According the BDW, Φ_j contains a Riesz basis with full rank spanning the subspace of level j, which is biorthogonal.

The wavelets are defined as differences of adjacent scaling functions: $\Psi_j = \Phi_{j-1} - \Phi_j$, with

$$\Psi_j = \Phi_{j-1} - \Phi_j, \ j = 1, 2, \ldots, \tag{8}$$

which are also locally supported. This formulation is fundamentally different from the DW and the BDW that acquire the wavelets from the complement space $(I - \Phi\Phi^*)$ via QR decomposition. According to (7) and (8), the wavelet $\psi_{j,x}$ has a zero mean

$$\sum_{y\in M} \psi_{j,x}(y) = 0, \tag{9}$$

which implies that it vanishes at the zero frequency in its Fourier transform.

The index j in the above-formulated functions associates with the "frequency" in spectral domain. Small values of j associate with high frequencies, while large values associate with low frequencies. As j increases, the scaling functions and wavelet functions dilate to larger areas rapidly because of the dyadic powers. For large enough values of j, the scaling functions and wavelets converge to constants

$$\varphi_{j,x} \to \frac{1}{A(M)}, \text{and } \psi_{j,x} \to 0, \tag{10}$$

where $A(M)$ denotes the total surface area of M.

Next, we will discuss the admissibility condition. This condition is for continuous wavelet transform originally in euclidean space. Here, we simply extend it to manifold space by the following definition. On manifold with bounded geometry, a wavelet ψ is *admissible*, or equivalently satisfies the *admissibility condition*, if $\sum_{k=0}^{\infty} \frac{|\mathcal{F}_\psi(k)|^2}{k} < \infty$, where $\mathcal{F}_\psi$ denotes the manifold harmonic transform of ψ. This definition is analogous to its origin in euclidean space, since the MHT is a manifold Fourier transform. The wavelets $\psi_{j,x}$ defined by (8) are admissible.

Proof. Recall that the zero-frequency MHB $\phi_0 = \frac{1}{\sqrt{A(M)}}$, which is a constant everywhere on M. According to (9), the wavelet $\psi_{j,x}$ has zero mean. Hence, it vanishes at zero frequency in its MHT,

$$\mathcal{F}_{\psi_{j,x}}(0) = \langle \psi_{j,x}, \phi_0 \rangle = 0.$$

Also, since the wavelet $\psi_{j,x}$ is compactly supported, it has limited bandwidth in its MHT. Assume that its upper frequency is $K(j)$. We then have

$$\mathcal{F}_{\psi_{j,x}}(k) = 0, \text{for } k > K(j).$$

Hence, we have

$$\sum_{k=0}^{\infty} \frac{|\mathcal{F}_{\psi_{j,x}}(k)|^2}{k} = \sum_{k=1}^{K(j)} \frac{|\mathcal{F}_{\psi_{j,x}}(k)|^2}{k} < \infty,$$

and hence, $\psi_{j,x}$ is admissible. □

In fact, by recalling [35], the zero-mean property of $\psi_{j,x}$ suffices the admissibility condition for compactly supported wavelets. This condition is critical for wavelet transform, as it ensures the transform can be fully recovered.

Fig. 2 illustrates some scaling functions and wavelets on a 1D manifold with 100 points. The diffusion wavelets are

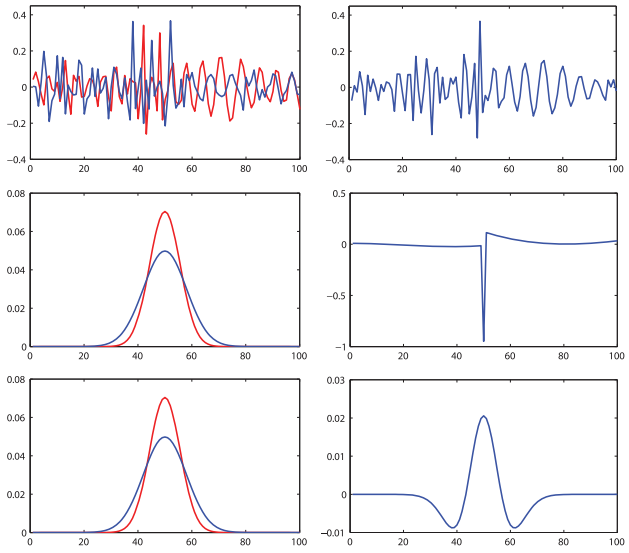

Fig. 2. Examples of the DW (*Top*), the BDW (*Middle*), and the ADW (*Bottom*) on a 1D manifold with 100 points. *Left*: scaling functions $\varphi_{9,50}$ (colored in red) and $\varphi_{10,50}$ (colored in blue). *Right*: wavelets $\psi_{10,50}$.

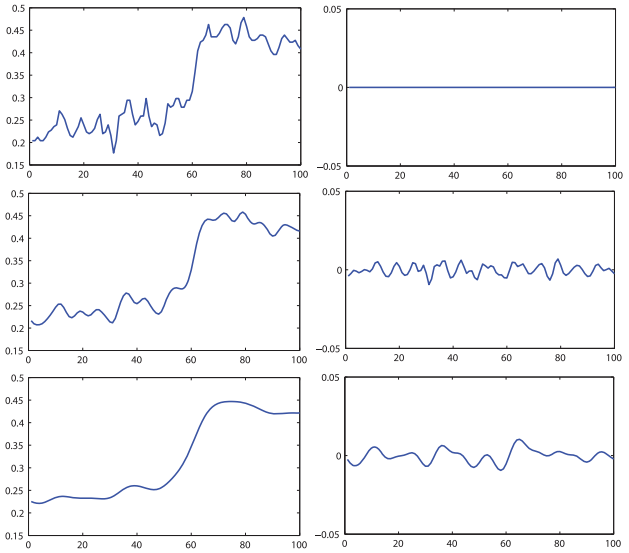

Fig. 4. Scaling (*Left*) and wavelet (*Right*) coefficients of a 1D function at $j = 0, 3, 6$. The function is smoothed by the scaling transform, with details recorded in the wavelet transform at different scales.

orthogonal yet not locally supported. The biorthogonal diffusion wavelets are locally supported, but not admissible. Our admissible wavelets are locally supported with oscillating and attenuated shapes. As j increases, the scaling functions dilate to larger areas. Fig. 3 visualizes a scaling function and a wavelet of the ADW on a meshed surface by color coding. The functions on surfaces have similar behaviors with that in the 1D case.

3.3 Transform and Reconstruction

Transform. The scaling and wavelet transforms (denoted by $\mathcal{S}_f$ and $\mathcal{W}_f$, respectively) of a function $f(x)$ with $x \in M$ are computed by the inner product over the domain M:

$$\mathcal{S}_f(j,x) = \langle f, \varphi_{j,x} \rangle, \ \mathcal{W}_f(j,x) = \langle f, \psi_{j,x} \rangle, \tag{11}$$

where j and x localize the frequency domain and the space domain, respectively. The scaling coefficient $\mathcal{S}_f(j,x)$ is a smoothed representation of function f, which is an approximation to f at scale j. The wavelet coefficient $\mathcal{W}_f(j,x)$ records the residual detailed information of f with respect to the scale j. Fig. 4 illustrates some scaling and wavelet coefficients of a 1D function. The function is smoothed by the scaling transform, with details recorded in the wavelet transform at different scales. In Fig. 5, a shape and a scalar field (mean curvature map) on the shape are transformed to different scales by our scaling transform. The scaling coefficients become constant everywhere at the coarsest scale. This indicates that the function space is highly compressible after scaling transforms, as it is gradually smoothed. In our applications, we retain full resolution of the scaling and wavelet transform, with our emphasis on accurate high-frequency processing. For applications with other purposes such as level-of-details rendering and function approximation, one could compress the scaling coefficients (i.e., smoothed functions) via downsampling.

Reconstruction. The reconstruction (inverse transform) aims to recover a function from its coefficients. For the DW, the reconstruction uses the same basis as the transform, since it is orthogonal and complete. The scaling functions of the BDW form a Riesz basis. According to [36], if $\{\varphi_i\}$ is a Riesz basis, there is a unique dual basis $\{\widetilde{\varphi}_j\}$ that is orthogonal to $\{\varphi_i\}$:

$$\langle \varphi_i, \widetilde{\varphi}_j \rangle = \delta_{ij}, \tag{12}$$

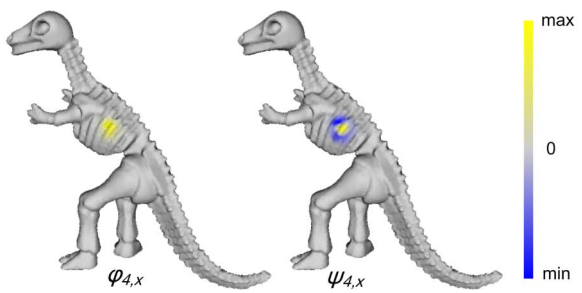

Fig. 3. Rendering a scaling function and a wavelet of the ADW on a meshed surface by color coding. Please pay attention to the similarity with the functions in the 1D case.

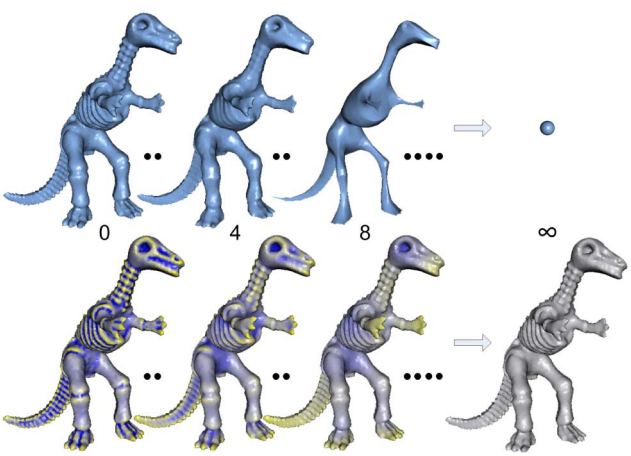

Fig. 5. Multiscale representations of a shape (top) and a scalar field defined on the shape (bottom) by our scaling transform. The scaling coefficients become constant everywhere at the coarsest scale.

TABLE 1
Comparison of the DW, the BDW, and the ADW

	DW	BDW	ADW
Orthogonality	Orthogonal	Biorthogonal	Biorthogonal[1]
Locally-supported	No	Yes	Yes
Admissible	No	No	Yes
Reconstruction	Orthogonal	Biorthogonal	Rapid

and $\{\varphi_i\}$ is biorthogonal. The reconstruction is given by [20]

$$f = \sum_{x \in M} \langle f, \varphi_{j,x} \rangle \widetilde{\varphi}_{j,x}, \tag{13}$$

where $\{\widetilde{\varphi}_{j,x}\}$ is the dual basis of $\{\varphi_{j,x}\}$. This requires the scaling matrix Φ_j to have full rank. Therefore, the rank-revealing QR decomposition is necessary. The dual basis is computed by the matrix inverse

$$\Phi_j \widetilde{\Phi}_j = I. \tag{14}$$

The QR decomposition and matrix inverse are computed at each level, which make the reconstruction computationally expensive.

Different from the DW and the BDW, we adopt a rapid reconstruction, which is a superposition of wavelet and scaling coefficients. According to the definition of our wavelets, we have

$$\begin{aligned} \mathcal{W}_f(j,x) &= \langle f, \psi_{j,x} \rangle \\ &= \langle f, \varphi_{j-1,x} - \varphi_{j,x} \rangle \\ &= \mathcal{S}_f(j-1,x) - \mathcal{S}_f(j,x), \end{aligned}$$

for $j = 1, 2, \ldots$ This implies that the wavelet coefficients are full-resolution details at different levels of frequencies. The function can be rapidly reconstructed by a series of J levels of wavelet coefficients $\{\mathcal{W}_f(j)\}_{j=1}^{J}$ and a scaling coefficient at the coarse level $\mathcal{S}_f(J)$

$$f(x) = \mathcal{S}_f(0,x) = \mathcal{S}_f(J,x) + \sum_{j=1}^{J} \mathcal{W}_f(j,x). \tag{15}$$

Since all the coefficients have full resolution, the rapid reconstruction is lossless.

4 Relations and Implementation

This section highlights the unique characteristics of the ADW by revealing intrinsic relations with other relevant techniques, and portrays the implementation mechanism.

Relations to diffusion wavelets. The proposed construction operator in (1) is a diffusion operator. Thus, it can be placed to the family of diffusion wavelets. As shown in Fig. 2, the DW impose orthogonalization on scaling functions and wavelets, which, however, are not locally supported. The BDW release this requirement for scaling functions to make them locally supported. The wavelets still form an orthogonal basis for the complement space $(I - \Phi\Phi^*)$. Neither the DW nor the BDW are admissible. The admissibility condition produces nice shapes of the wavelets, as the one of our ADW shown in the bottom right of Fig. 2. For reconstruction, the DW recover the function by their orthogonal basis; the BDW achieve the same goal by the biorthogonal dual basis; our rapid reconstruction does not rely on any basis. This characteristic is documented in Table 1.[1]

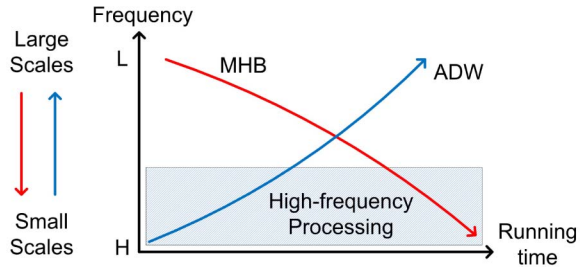

Fig. 6. The construction of the MHB uses a top-down approach starting from large scales to small scales. Low-frequency basis is fast to compute, while high-frequency basis is time consuming. On the contrary, the construction of the ADW adopts a bottom-up approach, where high-frequency basis is fast to compute. Therefore, the ADW are more efficient for high-frequency processing in shape analysis.

Relation to the MHB. Analogous to sine/cosine functions in Fourier transform, manifold harmonics are global functions on manifolds, which support spectral analysis of functions in $L^2(M)$. The construction of MHB follows a top-down approach that starts from large scales to small scales. Low-frequency basis functions are fast to compute, while high-frequency basis functions are time consuming. On the contrary, the construction of the ADW adopts a bottom-up approach, where high-frequency basis functions are fast to compute. From the perspective of running time, the ADW are more efficient for high-frequency processing in spectral analysis. This feature is explained in Fig. 6. The reconstruction of MHT is lossless only if the entire spectrum of all eigenfunctions is utilized, which is extremely expensive to compute. The common practice for MHT is that, high-frequency basis functions are oftentimes ignored, leading to lossy reconstruction and information processing. The MHT is easy to manipulate shape signals in low frequencies, while operations in high frequencies always consume extremely high computational cost. In sharp contrast, the reconstruction of the ADW has an "inverse" procedure that starts from high frequencies, leaving low-frequency components in the scaling coefficients at the coarsest level. This bottom-up approach makes it extremely attractive and powerful when processing shape signals in fine, local details.

Relation to spectral graph wavelets. This paragraph addresses the relation to wavelets built on graphs via spectral graph theory [32]. The spectral graph wavelets are constructed using the graph Fourier transform. In graph Fourier domain, the wavelets have explicit formulations generated by a kernel and dilated by time t. When applied to manifold data, a similar construction can be expected using the manifold harmonics transform. It leads to a generic mechanism for generating continuous wavelets. If one chooses a diffusion kernel (e.g., the heat kernel) to generate the wavelets, they will be similar with the ADW in function shape and application effects. The construction of spectral graph wavelets requires MHB, and hence, the eigen-decomposition of the Laplace-Beltrami operator, which is costly to compute. There is a similar feature with the MHB

1. The scaling functions and wavelets of the ADW can be made biorthogonal by downsampling the subspaces to match with ranks of basis matrices.

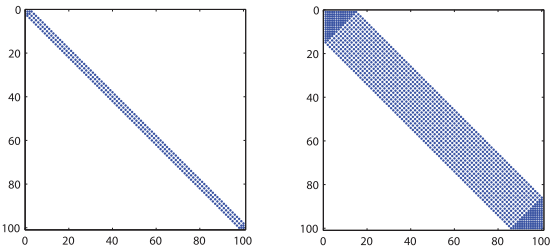

Fig. 7. Sparse matrices Φ_1 and Φ_4 in Fig. 2.

that, the spectral graph/manifold wavelets are more time consuming in processing high-frequency details.

Relation to differential coordinates. Differential coordinates [37] have been extensively studied and applied to fast mesh editing. The Laplacian operator is a linear operator that captures details of a surface. Given the divergence of the vector field b, the scalar field f can be reconstructed by solving the Poisson equation [38] $\Delta f = b$, which gives rise to a sparse linear system. Our wavelet transform $\mathcal{W}_f(1,x)$ has very similar behaviors, since the wavelet basis Ψ_1 is a differential operator with entries

$$\begin{cases} \Psi_1(x,y) = -\dfrac{\mathbf{T}(x,y)}{2\mathbf{T}(x,x)} \\ \Psi_1(x,x) = -\sum_x \Psi_1(x,y) = \frac{1}{2}, \end{cases} \tag{16}$$

where $\mathbf{T}(x,x) = \sum_y \mathbf{T}(x,y)$ as defined in (1). When the field f is a function of coordinates, $\mathcal{W}_f(1,x)$ is a representation of differential coordinates. For wavelet transform at high frequencies, they behave exactly like differential coordinates in larger neighborhood [39].

Implementation. In this work, time performance is considered as an important criterion for algorithm design. Algorithm 1 documents the construction of scaling functions and wavelets of the ADW. For a given data (mesh or point cloud) M, our method first computes the local operator $\mathbf{T}$. Then, it initializes the first level of scaling functions Φ_1 and wavelets Ψ_1, stored as sparse matrices. The following levels of scaling functions are computed by sparse matrix multiplication of previous levels, subject to normalization and a threshold ϵ. Finally, the differences of two adjacent scaling functions form the wavelets. The computation of ADW is mainly on nonzero entries of sparse matrices. We use Matlab to compute the operations of sparse matrices, whose complexity is linear to the number of nonzero elements. Assume the number of vertices is n, and for all $x \in M$, the operator $\mathbf{T}(x,\cdot)$ has at most constant m entries. The time complexity for computing j levels of ADW on a d-dimensional manifold is $O(2^{dj}n)$. The amount of computation will be huge for even moderate values of j. Since we are particularly interested in high-frequency processing of spectral analysis, a small value of $j \leq 8$ is sufficient for our applications. In this case, Φ_j and Ψ_j continue to be sparse matrices. To ensure the numerical sparsity, ignorable elements are eliminated by a threshold $\epsilon = 10^{-6}$ before the row-based normalization. Fig. 7 visually depicts the structure of the sparse matrices Φ_1 and Φ_4 of the 1D example shown in Fig. 2. The matrices are sparser for data with more points. For other applications that need to access lower frequencies, one could downsample the scaling transforms to reduce computation.

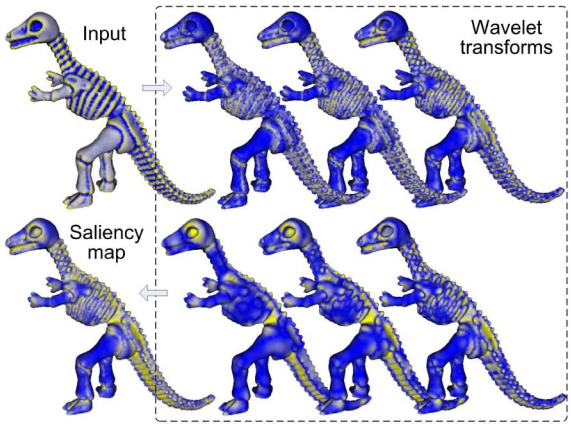

Fig. 8. The saliency map of an input function is the nonlinear sum of its wavelet coefficients.

Algorithm 1: Computation of scaling functions and wavelets of the ADW.

Input: data M, levels J
Output: basis $\{\Phi_j\}_{j=0}^{J}$, $\{\Psi_j\}_{j=1}^{J}$

compute operator $\mathbf{T}$;
$\Phi_0 = \{\delta_x\}_{x\in M}$, $\Phi_1 = [\Phi_0\mathbf{T}]_r$;
$\Psi_1 = \Phi_0 - \Phi_1$;
for $j = 1 : J$ **do**
  $\Phi_j = [\Phi_{j-1}\Phi_{j-1}]_{r,\epsilon}$;
  $\Psi_j = \Phi_{j-1} - \Phi_j$;
end

5 Applications and Results

We conduct experiments and showcase several important applications of our method, including saliency visualization, multiscale feature definition and extraction, and geometry processing, with time performance explicitly documented at the end of this section.

5.1 Saliency Visualization

In [40], Lee et al. defined the saliency map as the difference of two Gaussian convoluted scalar fields of a curvature map, and the mesh saliency as the nonlinear combination of the saliency maps in multiple scales. As a useful tool, it has been applied to mesh simplification [40], volume visualization [41], feature matching [42], visual perception [43], etc.

The proposed ADW have similar effects. For a given function f, its wavelet coefficients encode the saliency information of multiscale details. Analogous to [40], the saliency map is computed by the nonlinear sum of wavelet coefficients at different scales

$$\Lambda(f) = \sum_j \alpha_j |\mathcal{W}_f(j)|, \tag{17}$$

where $\alpha_j = (\max(|\mathcal{W}_f(j)|) - \overline{|\mathcal{W}_f(j)|})^2$ is a coefficient. Fig. 8 shows the workflow of computing the saliency map by using the ADW. To avoid being affected by noise perturbation, the first two levels of $\mathcal{W}_j$ are ignored. The wavelet coefficients capture the changes of the function at different scales. Low-frequency wavelets capture small-scale changes, while high-frequency ones capture large-scale changes.

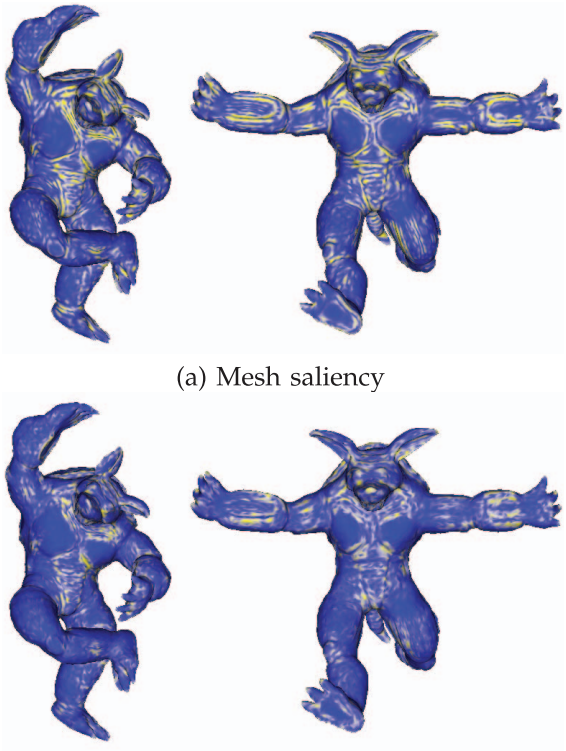

(a) Mesh saliency

(b) ADW

Fig. 9. Comparison of saliency maps on two deformed shapes of the Armadillo: the mesh saliency in [40] (a) and the ADW (b).

Fig. 9 shows the saliency maps of mean curvature maps on two deformed shapes of the Armadillo, where the top row is the result of Lee et al. [40] and the bottom row is our result. The original mesh saliency in [40] is computed by an euclidean Gaussian. In general, the two methods both adopt the *difference-of-Gaussian* operator, and therefore, they have similar effects in saliency visualization. The setting of the mesh saliency in multiscale Gaussian is more empirical, while the ADW have a rigorous construction by means of wavelets. They have some differences in counting saliency components at different scales. We also compute saliency maps by the ADW from other functions on the shape, such as texture, and vertex coordinates. Figs. 11 and 12 show saliency maps of texture on meshed surfaces and coordinates on point clouds, respectively.

5.2 Multiscale Feature Definition and Extraction

Feature definition and extraction plays a critical role in many graphics and visualization tasks. Shape features are oftentimes interpreted as local extrema of a scalar field of saliency, with the help of diffusion for multiscale detection. In [44], geometric and texture features are found by a scale space with geodesic metric. In [45], a feature map is defined by a discrete heat kernel on triangular meshes, with which multiscale critical points can be found as features. And in [46], anisotropic diffusion is adopted in this mechanism. As the fundamental solution to the heat equation on manifolds, the heat kernel itself contains saliency information, which is used for feature extraction based on the heat kernel signature in [47].

The essence of multiscale feature extraction is to construct multiscale approximations for a signal through diffusion, and find maximum changes in the scale space [48]. This can be easily incorporated with the ADW, since the wavelet transform operates on the difference between two smoothed representations. Specifically, given a function f (e.g., coordinates, texture, curvature map, or density), its scaling coefficients $\{S_f(j)\}$ form the scale space of f with respect to j. Its wavelet coefficients are the first-order derivatives of the scale space. Therefore, the scale space is a 3D manifold with scale ("frequency") j as the third dimension. Analogous to [48], the ADW seek features as local extrema in this 3D manifold space. More specifically, a point x is recognized as a feature if it is an extremum in its local neighborhood in a complex space-frequency domain. In spatial domain, the neighborhood of a vertex contains its two-ring neighbors for meshed surface or 10 nearest neighbors for point clouds. In frequency domain, the neighborhood is two adjacent levels of scales. This algorithm is documented in Algorithm 2. It has a parameter θ so that only features with $|W_f(j,x)| > \theta\,\overline{|\mathcal{W}_f(j)|}$ are actually selected. We use $\theta = 2.4$ as a default, while allowing fine tuning in the range of $[1.6, 3.0]$ in our experiments.

Algorithm 2: Feature extraction by ADW.

Input: data M, function f, levels J, threshold θ
Output: feature sets F

compute $\{\Psi_j\}_{j=1}^{J}$ by Algorithm 1;
for $j = 1 : J$ **do**
  $\mathcal{W}_f(j,x) = \langle \psi_{j,x}, f \rangle$;
end
for $j = 2 : J-1$ **do**
  for $x \in M$ **do**
    if $|\mathcal{W}_f(j,x)| < \theta\,\overline{|\mathcal{W}_f(j)|}$ **then**
      continue;
    end
    for y *in the neighbor of* x **do**
      if $\mathcal{W}_f(j,x) > \mathcal{W}_f(j,y)$ &&
      $\mathcal{W}_f(j,x) > \mathcal{W}_f(j-1,y)$ &&
      $\mathcal{W}_f(j,x) > \mathcal{W}_f(j+1,y)$ **then**
        Insert x into F;
      else if $\mathcal{W}_f(j,x) < \mathcal{W}_f(j,y)$ &&
      $\mathcal{W}_f(j,x) < \mathcal{W}_f(j-1,y)$ &&
      $\mathcal{W}_f(j,x) < \mathcal{W}_f(j+1,y)$ **then**
        Insert x into F;
      end
    end
  end
end

In Fig. 10, extracted features of vertex coordinates are shown as green balls with their sizes corresponding to their correct scales. The threshold θ controls the number of features, according to their values of saliency. Features with greater values of wavelet coefficients are more salient, thus, more stable. Fig. 10 also shows an experiment with noisy input. We add Gaussian noise with increasing standard deviation σ of mean edge length in normal directions. Large-scale features appear to be more stable than small-scale features. Even with large noise (50 percent), one can still find stable features at the larger scales, which are exactly the same as that on the noise-free shape. Figs. 11 and 12 show more

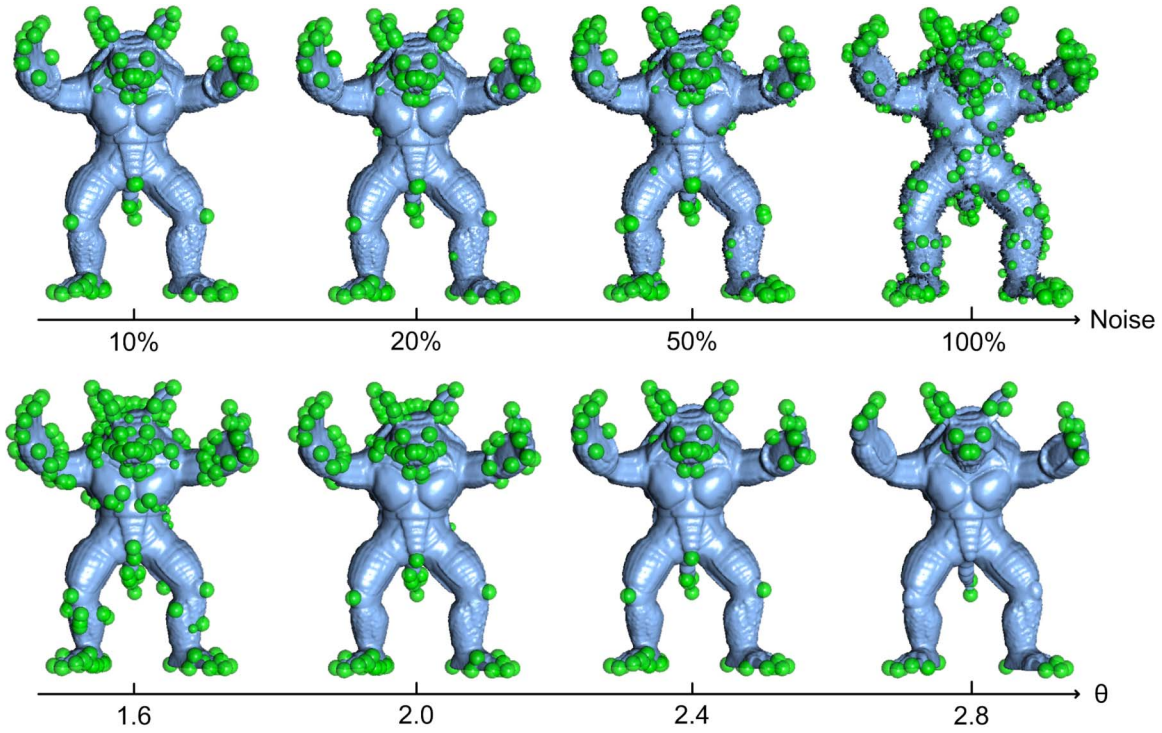

Fig. 10. Feature detection on the Armadillo with different thresholds θ and Gaussian noise with increasing σ of mean edge length in normal directions. Features are rendered by green balls with their sizes representing correct scales. We fix $\theta = 2.4$ in the noise experiment. Large-scale features are more stable than small-scale features.

results on textures and point clouds. The ADW can rapidly find rich features from the scale space. Textures on meshed surfaces have information other than shape geometry, which is capable of finding features in areas with indistinctive shape but rather rapidly changing texture. We also conduct a comparison with the feature map in [45] in Fig. 11, which finds critical points at multiscale approximations of the input function. The critical points found by the feature map (*Left*) have zero first derivatives of smoothed approximation. The wavelet transform of ADW (*Right*) extracts multiscale details of the input function, and finds features as zero crossings of second-order derivatives in its multiscale representation. For point clouds in Fig. 12, we directly use point coordinates as input functions f_i, where $i = 1, 2, 3$. The wavelet coefficients in three dimensions are consolidated together by $\mathcal{W}_f(j,x) = \|\mathcal{W}_{f_i}(j,x)\|_2$. In these experiments, we choose not to apply feature filters, for instance edge filter and boundary filter that could eliminate features on edges and boundaries, respectively. Depending on the purpose of feature extraction in different practice, these filters can be easily introduced and take appropriate actions.

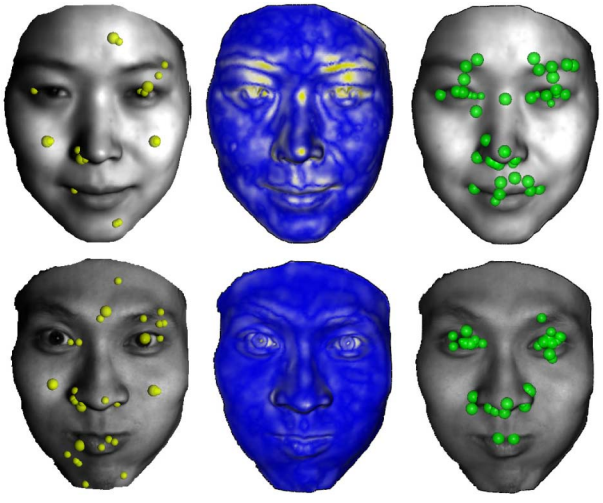

Fig. 11. Saliency maps and extracted features of input textures, from *Left* to *Right*: critical points by the feature map in [45], saliency maps by ADW, and feature extraction by ADW.

5.3 Spectral Geometry Processing

As powerful spectral tools, the ADW enable geometry analysis and synthesis at different frequencies and places, by filtering their wavelet coefficients. In this application, the vertex coordinates are taken as the function f. Since the vertex coordinate is a 3D vector, its three components are treated independently. For a given mesh, we compute scaling and wavelet coefficients of its vertex coordinates. Then, we apply filters on the wavelet coefficients to process the geometry. The output mesh can be recovered from a series of wavelet coefficients $\{W_f(j)\}_{j=1}^{J}$ and a scaling coefficient $S_f(J)$ at the coarsest level, using the rapid reconstruction formulated in (15). Unlike the MHT that is an analogue of Fourier transform, the ADW can afford local operations during geometry analysis and processing. This can be done instantly by applying space-frequency filters $\Gamma(j,x)$. The rapid reconstruction of processed coefficients can be formulated as

$$f(x) = S_f(J,x) + \sum_{j=1}^{J} \Gamma(j,x) W_f(j,x). \tag{18}$$

Accordingly, we name $\Gamma(j,x)$ as a *global* filter if it is equally applied to all $x \in M$, and a *local* filter if applied to a

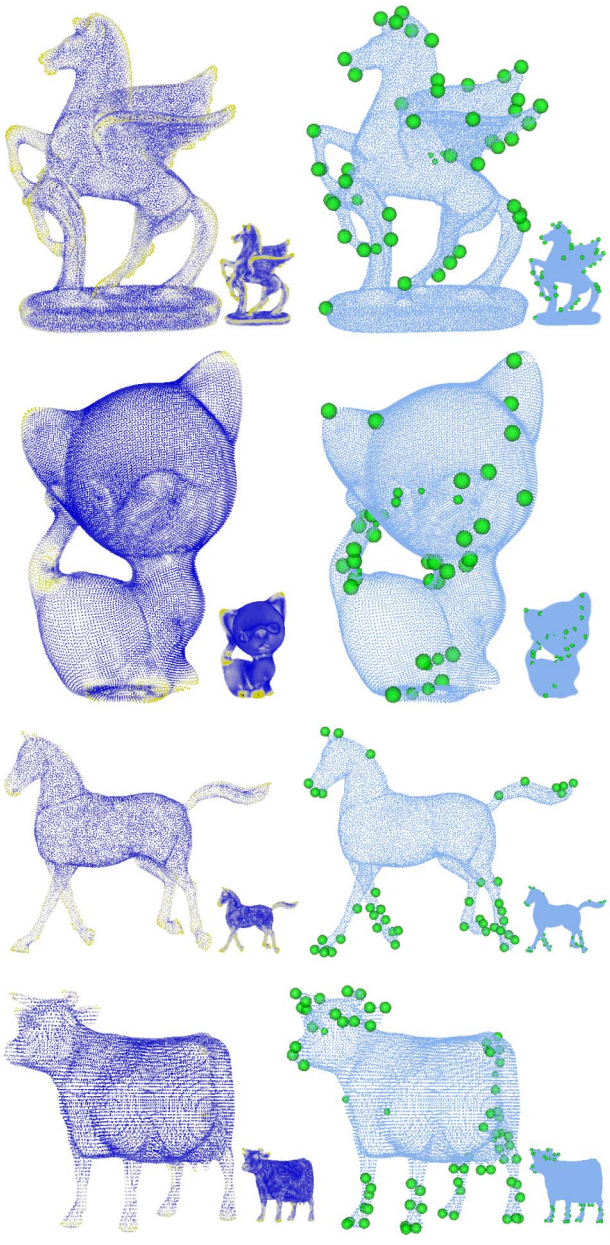

Fig. 12. Saliency visualization and feature detection on point clouds.

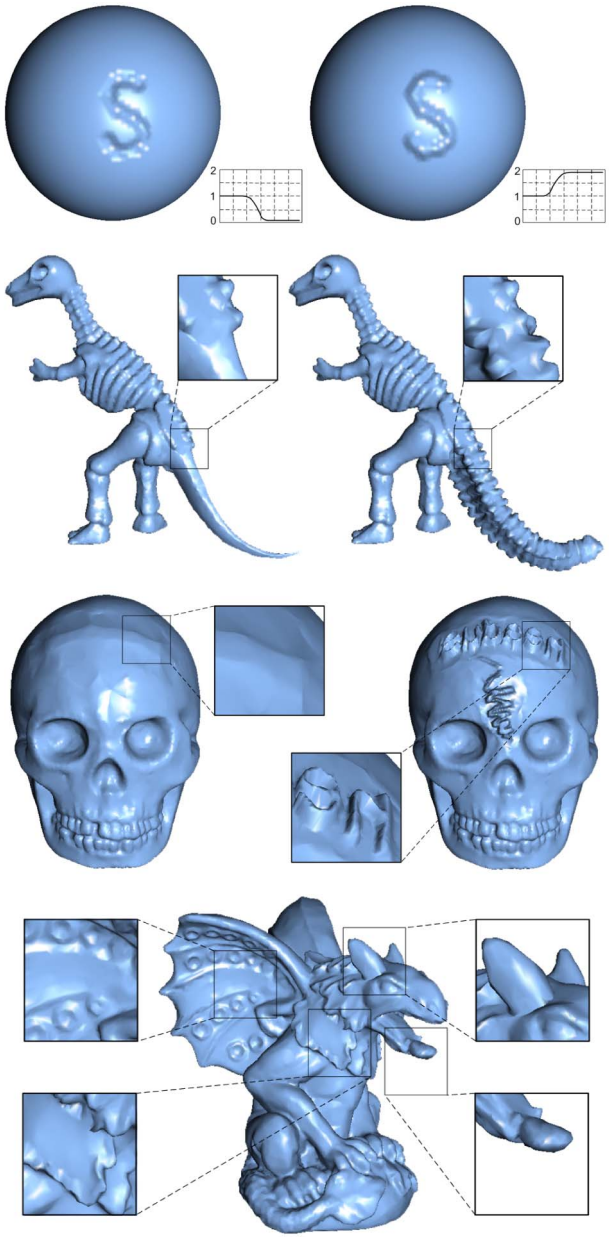

Fig. 13. Local geometry processing: suppression (*Left*) and enhancement (*Right*) on selected regions.

subset of M. In Figs. 13 and 14, we demonstrate the results of local and global filters. The local filters are associated with some selected regions, with results shown in Fig. 13. In the first example, we carve a letter "S" on a sphere by simply filtering the region selected by hand drawing. It results in a concave shape and a convex shape by the suppression filter and enhancement filter, respectively. The other examples follow the same way by applying space-frequency filters on selected regions, which generates a family of different effects on one shape through a sequence of filtering operations. On the model Gargoyle, selected areas at the wing and the neck are smoothed, while one horn and the tongue tip are enhanced. The entire processing pipeline can be carried out more efficiently if only the first few frequencies are involved, leading to operations on detail levels. Fig. 14 shows geometry processing using different types of global filters: suppression, enhancement, and band. In our framework, the shape geometry can be efficiently filtered, resulting in different effects. The suppression filter smoothes the shape by eliminating the details. On the contrary, the enhancement filter magnifies the details. The two band filters combine the suppression and enhancement in different scales. One smoothes the shape at some intermediate scales while keeping fine details. The other enhances the shape at some intermediate scales while smoothing fine details. Finally, we compare global geometry processing by ADW and manifold harmonics in Fig. 15. The two methods achieve similar results in global geometry processing, while the ADW can further perform local processing as shown in Fig. 13.

5.4 Time Performance

We examine the time efficiency of our method in the applications, with performance documented in Table 2. The prototype software was developed on a laptop with

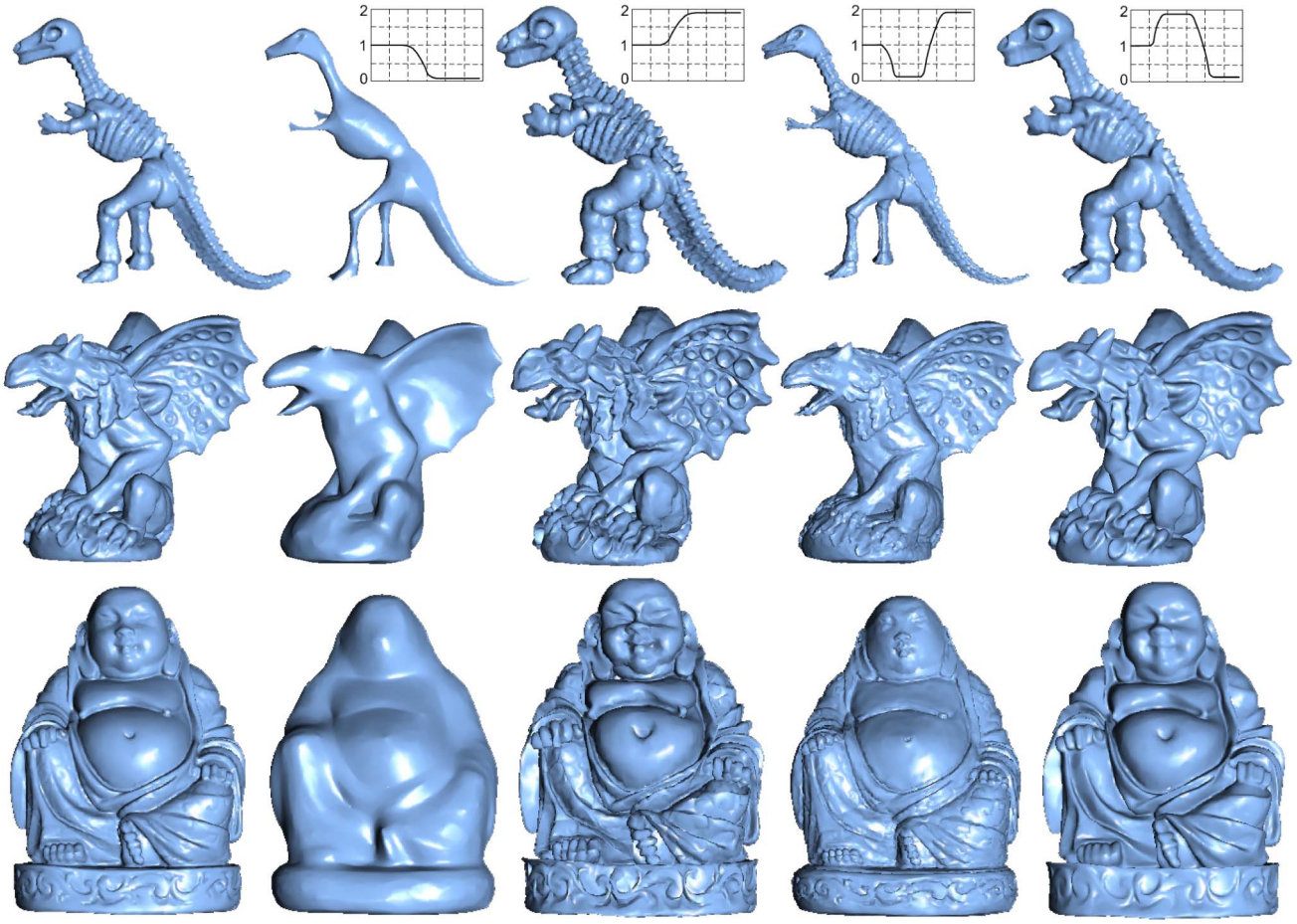

Fig. 14. Global geometry processing.

Core2 Duo CPU 2.53 GHz and 4 GB RAM. In each experiment, we record the computation time of the wavelet system $\{\Phi_j, \Psi_j\}$ denoted as "ADW," and the processing time for its application. The computation of ADW, depending on the number of points and the number of levels, is very efficient that can afford rapid spectral analysis. In saliency visualization, the processing time is to compute wavelet transforms and the saliency map. In multiscale feature extraction, it is to perform Algorithm 2. And in geometry processing, it is to compute the rapid reconstruction.

6 Discussion and Conclusion

We have detailed the admissible diffusion wavelets as powerful and effective tools for space-frequency processing with a suite of applications in visual computing. The ADW are constructed in a bottom-up manner, which starts from a local operator **T** and expands as its dyadic powers increase. We have formulated the scaling functions and wavelets (that are also locally supported) in a mathematically rigorous way. The admissibility condition is naturally enforced by the

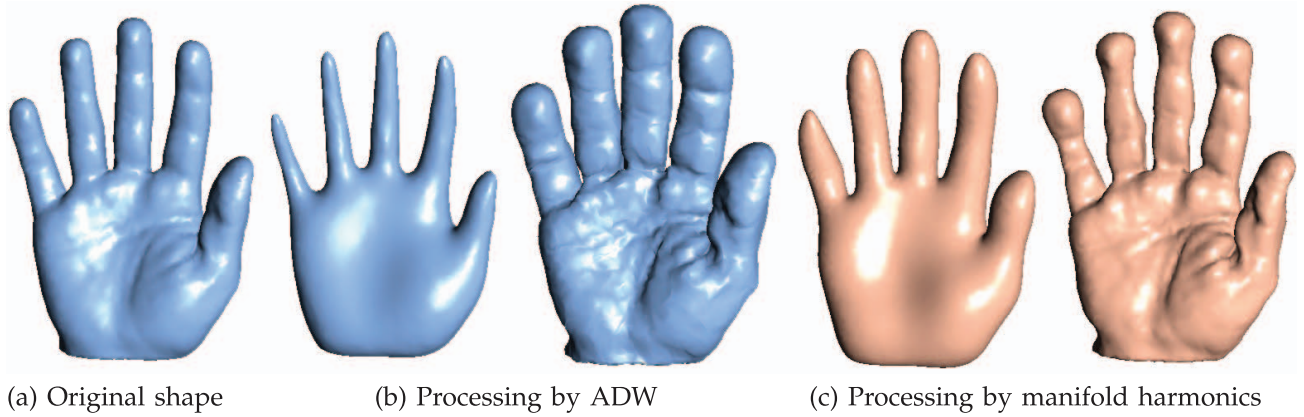

Fig. 15. Comparison of global geometry processing by ADW (b) and manifold harmonics (c).

TABLE 2
Time Performance of Our Method (in Seconds)

Data	# V	J	ADW	Processing
Dinosaur (Fig. 8)	14053	8	35.03	0.03
Armadillo (Fig. 10)	50000	6	30.61	5.52
Face (Fig. 11)	10156	5	1.67	0.47
Pegaso (Fig. 12)	30000	4	7.12	1.25
Kitten (Fig. 12)	28969	4	4.09	1.18
Horse (Fig. 12)	10296	4	1.70	0.39
Cow (Fig. 12)	16612	4	3.11	0.62
Sphere (Fig. 13)	10242	8	30.34	0.05
Skull (Fig. 13)	20002	7	19.39	0.11
Gargoyle (Fig. 14)	25011	7	28.63	0.11
Buddha (Fig. 14)	25003	7	30.15	0.12
Hand (Fig. 15)	10000	7	14.66	0.05

definition of wavelets. The rapid reconstruction is carried out by employing coefficients, located at multiple frequencies. The dyadic power series $\mathbf{T}^{2^j}$ efficiently scales the Hilbert space. As j increases, the ADW collect valuable information from small scales, propagate that to large scales, and continue to spread through the hierarchy. The rapid computation of sparse ADW at the first several levels of scales, make them very efficient for high-frequency processing. For processing in low frequencies (i.e., large scales), the computational efficiency might become moderate. Therefore, it makes sense to concentrate on high-frequency-relevant applications such as saliency visualization, feature definition and extraction, and geometry analysis and processing. In practice, since the dyadic power grows very fast, several levels of ADW appear to be adequate for our applications, where the computation is significantly faster than solving the global eigen-system. More importantly, spatial localization of wavelets empowers the ADW to have the unique characteristic of space-frequency processing toward seeking local features and filtering local geometry, while retaining gross shape globally.

We have shown that the ADW can be computed on both meshes and point clouds, which only involves local geometry. Therefore, it can be directly generalized to handle other data domains such as graphs with discrete structure, tensor fields defined over multidimensional volume, and even higher dimensional scientific data with curved manifold structure. Our ongoing and near-future research endeavors are undertaken toward broadening the application scope, with special emphases on space-time dynamic data modeling and analysis, data manipulation, and shape editing and deformation.

ACKNOWLEDGMENTS

This research is supported in part by the US National Science Foundation (NSF) grants IIS-0710819, IIS-0949467, IIS-1047715, and IIS-1049448. Models are courtesy of the AIM@SHAPE repository.

REFERENCES

[1] I. Drori and D. Lischinski, "Fast Multiresolution Image Operations in the Wavelet Domain," *IEEE Trans. Visualization and Computer Graphics,* vol. 9, no. 3, pp. 395-411, July-Sept. 2003.

[2] M.A.T. Figueiredo, "Bayesian Image Segmentation Using Wavelet-Based Priors," *Proc. IEEE CS Computer Vision and Pattern Recognition,* pp. 437-443, 2005.

[3] R.S. Overbeck, C. Donner, and R. Ramamoorthi, "Adaptive Wavelet Rendering," *ACM Trans. Graphics,* vol. 28, no. 5, pp. 140:1-140:12, 2009.

[4] L. Lippert and M.H. Gross, "Fast Wavelet Based Volume Rendering by Accumulation of Transparent Texture Maps," *Computer Graphics Forum,* vol. 14, no. 3, pp. 431-444, 1995.

[5] G. Craciun, M. Jiang, D. Thompson, and R. Machiraju, "Spatial Domain Wavelet Design for Feature Preservation in Computational Data Sets," *IEEE Trans. Visualization and Computer Graphics,* vol. 11, no. 2, pp. 149-159, Mar./Apr. 2005.

[6] J.C. de Iehl and B. Péroche, "An Adaptive Spectral Rendering with a Perceptual Control," *Computer Graphics Forum,* vol. 19, no. 3, pp. 291-300, 2000.

[7] L. Olsen, F.F. Samavati, and R.H. Bartels, "Multiresolution for Curves and Surfaces Based on Constraining Wavelets," *Computers and Graphics,* vol. 31, no. 3, pp. 449-462, 2007.

[8] F. Payan and M. Antonini, "Mean Square Error Approximation for Wavelet-Based Semiregular Mesh Compression," *IEEE Trans. Visualization and Computer Graphics,* vol. 12, no. 4, pp. 649-657, July/Aug. 2006.

[9] F. Payan and M. Antonini, "Temporal Wavelet-Based Compression for 3D Animated Models," *Computers and Graphics,* vol. 31, no. 1, pp. 77-88, 2007.

[10] B. Vallet and B. Lévy, "Spectral Geometry Processing with Manifold Harmonics," *Computer Graphics Forum,* vol. 27, no. 2, pp. 251-260, 2008.

[11] I. Guskov, W. Sweldens, and P. Schröder, "Multiresolution Signal Processing for Meshes," *Proc. ACM SIGGRAPH,* pp. 325-334, 1999.

[12] M. Bertram, M.A. Duchaineau, B. Hamann, and K. Joy, "Bicubic Subdivision-Surface Wavelets for Large-Scale Isosurface Representation and Visualization," *Proc. IEEE Conf. Visualization,* pp. 389-396, 2000.

[13] M. Bertram, M.A. Duchaineau, B. Hamann, and K.I. Joy, "Generalized B-Spline Subdivision-Surface Wavelets for Geometry Compression," *IEEE Trans. Visualization and Computer Graphics,* vol. 10, no. 3, pp. 326-338, May/June 2004.

[14] G.-P. Bonneau, "Optimal Triangular Harr Bases for Spherical Data," *Proc. IEEE Visualization,* pp. 279-284, 1999.

[15] C. Lessig and E. Fiume, "Soho: Orthogonal and Symmetric Haar Wavelets on the Sphere," *ACM Trans. Graphics,* vol. 27, no. 1, pp. 4:1-4:11, 2008.

[16] M. Lounsbery, T.D. DeRose, and J. Warren, "Multiresolution Analysis for Surfaces of Arbitrary Topological Type," *ACM Trans. Graphics,* vol. 16, no. 1, pp. 34-73, 1997.

[17] G.M. Nielson, I.-H. Jung, and J. Sung, "Haar Wavelets over Triangular Domains with Applications to Multiresolution Models for Flow over a Sphere," *Proc. IEEE Visualization,* pp. 143-150, 1997.

[18] S. Valette and R. Prost, "Wavelet-Based Multiresolution Analysis of Irregular Surface Meshes," *IEEE Trans. Visualization and Computer Graphics,* vol. 10, no. 2, pp. 113-122, Mar./Apr. 2004.

[19] R.R. Coifman and M. Maggioni, "Diffusion Wavelets," *Applied and Computational Harmonic Analysis,* vol. 21, no. 1, pp. 53-94, 2006.

[20] M. Maggioni, J. Bremer, R.R. Coifman, and A. Szlam, "Biorthogonal Diffusion Wavelets for Multiscale Representations on Manifolds and Graphs," *Proc. SPIE Wavelets XI,* vol. 5914, pp. 1-13, 2005.

[21] M. Pauly and M. Gross, "Spectral Processing of Point-Sampled Geometry," *Proc. ACM SIGGRAPH,* pp. 379-386, 2001.

[22] Z. Karni and C. Gotsman, "Spectral Compression of Mesh Geometry," *Proc. ACM SIGGRAPH,* pp. 279-286, 2000.

[23] R. Kolluri, J.R. Shewchuk, and J.F. O'Brien, "Spectral Surface Reconstruction from Noisy Point Clouds," *Proc. Symp. Geometry Processing,* pp. 11-21, 2004.

[24] M. Ben-Chen and C. Gotsman, "On the Optimality of Spectral Compression of Mesh Data," *ACM Trans. Graphics,* vol. 24, no. 1, pp. 60-80, 2005.

[25] B. Lévy, "Laplace-Beltrami Eigenfunctions towards an Algorithm that "Understands" Geometry," *Proc. Int'l Conf. Shape Modeling and Applications,* pp. 13-20, 2006.

[26] G. Rong, Y. Cao, and X. Guo, "Spectral Mesh Deformation," *The Visual Computer,* vol. 24, no. 7, pp. 787-796, 2008.

[27] I. Daubechies, I. Guskov, P. Schröder, and W. Sweldens, "Wavelets on Irregular Point Sets," *Philosophical Transactions of the Royal Soc. A,* vol. 357, no. 1760, pp. 2397-2413, 1999.
[28] H. Wang, K. Qin, and H. Sun, "$\sqrt{3}$-Subdivision-Based Biorthogonal Wavelets," *IEEE Trans. Visualization and Computer Graphics,* vol. 13, no. 5, pp. 914-925, Sept. 2007.
[29] M. Charina, C.K. Chui, and W. He, "Tight Frames of Compactly Supported Multivariate Multi-Wavelets," *J. Computational and Applied Math.,* vol. 233, no. 8, pp. 2044-2061, 2010.
[30] S. Mahadevan and M. Maggioni, "Value Function Approximation with Diffusion Wavelets and Laplacian Eigenfunctions," *Proc. Neural Information Processing Systems,* 2005.
[31] R.M. Rustamov, "On Mesh Editing, Manifold Learning, and Diffusion Wavelets," *Proc. IMA Int'l Conf. Math. of Surfaces XIII,* pp. 307-321, 2009.
[32] D.K. Hammond, P. Vandergheynst, and R. Gribonval, "Wavelets on Graphs via Spectral Graph Theory," *Applied Computational Harmonic Analysis,* vol. 30, no. 2, pp. 129-150, 2011.
[33] M. Belkin, J. Sun, and Y. Wang, "Discrete Laplace Operator on Meshed Surfaces," *Proc. ACM Symp. Computational Geometry,* pp. 278-287, 2008.
[34] M. Belkin, J. Sun, and Y. Wang, "Constructing Laplace Operator from Point Clouds in R^d," *Proc. ACM-SIAM Symp. Discrete Algorithms,* pp. 1031-1040, 2009.
[35] J.-P. Antoine and P. Vandergheynst, "Wavelets on the 2-Sphere: A Group-Theoretical Approach," *Applied Computational Harmonic Analysis,* vol. 7, pp. 262-291, 1999.
[36] O. Christensen, *An Introduction to Frames and Riesz Bases.* Birkhäuser, 2002.
[37] M. Alexa, "Differential Coordinates for Local Mesh Morphing and Deformation," *The Visual Computer,* vol. 19, nos. 2/3, pp. 105-114, 2003.
[38] Y. Yu, K. Zhou, D. Xu, X. Shi, H. Bao, B. Guo, and H.-Y. Shum, "Mesh Editing with Poisson-Based Gradient Field Manipulation," *Proc. ACM SIGGRAPH,* pp. 644-651, 2004.
[39] Y. Lipman, O. Sorkine, D. Cohen-Or, D. Levin, C. Rössl, and H.-P. Seidel, "Differential Coordinates for Interactive Mesh Editing," *Proc. Shape Modeling Int'l,* pp. 181-190, 2004.
[40] C.H. Lee, A. Varshney, and D.W. Jacobs, "Mesh Saliency," *ACM Trans. Graphics,* vol. 24, no. 3, pp. 659-666, 2005.
[41] Y. Kim and A. Varshney, "Saliency-Guided Enhancement for Volume Visualization," *IEEE Trans. Visualization and Computer Graphics,* vol. 12, no. 5, pp. 925-932, Sept./Oct. 2006.
[42] U. Castellani, M. Cristani, S. Fantoni, and V. Murino, "Sparse Points Matching by Combining 3D Mesh Saliency with Statistical Descriptors," *Computer Graphics Forum,* vol. 27, no. 2, pp. 643-652, 2008.
[43] Y. Kim, A. Varshney, D.W. Jacobs, and F. Guimbretière, "Mesh Saliency and Human Eye Fixations," *ACM Trans. Applied Perception,* vol. 7, no. 2, pp. 12:1-12:13, 2010.
[44] T. Hou and H. Qin, "Efficient Computation of Scale-Space Features for Deformable Shape Correspondences," *Proc. European Conf. Computer Vision,* no. 3, pp. 384-397, 2010.
[45] G. Patanè and B. Falcidieno, "Multi-Scale Feature Spaces for Shape Processing and Analysis," *Proc. Shape Modeling Int'l,* pp. 113-123, 2010.
[46] S. Wang, T. Hou, Z. Su, and H. Qin, "Multi-Scale Anisotropic Heat Diffusion Based on Normal-Driven Shape Representation," *The Visual Computer,* vol. 27, nos. 6-8, pp. 429-439, 2011.
[47] J. Sun, M. Ovsjanikov, and L. Guibas, "A Concise and Provably Informative Multi-Scale Signature Based on Heat Diffusion," *Proc. Symp. Geometry Processing,* pp. 1383-1392, 2009.
[48] D. Lowe, "Distinctive Image Features from Scale-Invariant Keypoints," *Int'l J. Computer Vision,* vol. 60, no. 2, pp. 91-110, 2004.

Tingbo Hou received the BS degree from the University of Science and Technology of China in 2004, and the ME degree from Chinese Academy of Sciences in 2007. He is currently working toward the PhD degree from the Department of Computer Science, Stony Brook University (SUNY at Stony Brook). His research interests include visual computing, shape analysis, shape matching/registration, surface reconstruction, data completion, geometric modeling, and computational photography. He is a student member of the IEEE.

Hong Qin received the BS and MS degrees in computer science from Peking University, China. He received the PhD degree in computer science from the University of Toronto. He is a professor of computer science in the Department of Computer Science, State University of New York, Stony Brook (Stony Brook University). During his years at the University of Toronto (UofT), he received UofT Open Doctoral Fellowship. He was also the recipient of US National Science Foundation (NSF) CAREER Award from the NSF, Honda Initiation Award, and Alfred P. Sloan Research Fellow by the Sloan Foundation. Currently, he serves as an associate editor for The Visual Computer, Graphical Models, and *Journal of Computer Science and Technology*. His research interests include geometric and solid modeling, graphics, physics-based modeling and simulation, computer-aided geometric design, human-computer interaction, visualization, and scientific computing. Detailed information about him can be found from his website: http://www.cs.sunysb.edu/~qin. He can be reached at qin@cs.sunysb.edu. He is a senior member of the IEEE.